

Article

Effect of Cast Defects on the Corrosion Behavior and Mechanism of UNS C95810 Alloy in Artificial Seawater

Xu Zhao ¹, Yuhong Qi ^{1,*}, Jintao Wang ¹, Zhanping Zhang ¹, Jing Zhu ², Linlin Quan ² and Dachuan He ²

¹ Department of Materials Science and Engineering, Dalian Maritime University, Dalian 116026, China; zx1988@dmlu.edu.cn (X.Z.); 18342299941@163.com (J.W.); zzp@dmlu.edu.cn (Z.Z.)

² Dalian Marine Propeller Co., Ltd., Dalian 116021, China; jingzhu2009@yeah.net (J.Z.); quanlinlin@163.com (L.Q.); xyz@dmpp.cn (D.H.)

* Correspondence: yuhong_qi@dmlu.edu.cn

Received: 21 March 2020; Accepted: 8 April 2020; Published: 10 April 2020



Abstract: To study the effect of cast defects on the corrosion behavior and mechanism of the UNS C95810 alloy in seawater, an investigation was conducted by weight loss determination, scanning electron microscopy (SEM), confocal laser scanning microscopy (CLSM), X-ray diffraction (XRD) and electrochemical testing of the specimen with and without cast defects on the surface. The results show that the corrosion rate of the alloy with cast defects is higher than that of the alloy without cast defects, but the defects do not change the composition of the resulting corrosion products. The defects increase the complexity of the alloy microstructure and the tendency toward galvanic corrosion, which reduce the corrosion potential from -3.83 to -86.31 mV and increase the corrosion current density from 0.228 to 0.23 $\mu\text{A}\cdot\text{cm}^{-2}$.

Keywords: nickel-aluminum bronze; cast defects; electrochemical corrosion; mechanism; microstructure

1. Introduction

Due to its good mechanical properties, corrosion fatigue resistance, corrosion resistance and cavitation resistance, Ni-Al bronze (NAB) has been widely used for marine components, such as ship propellers, pumps and valves [1–3]. NAB parts used in seawater are inevitably subject to corrosion by the seawater. To date, there are many studies on NAB corrosion behavior in seawater [1,3–8]. The results showed that an α phase corroded while a κ phase did not corrode in near-neutral seawater and 3.5% NaCl solution [1,8,9]. Neodo et al. [7] studied the corrosion behavior of NAB in a 3.5% NaCl solution with different pH values. It was found that the κ phase is preferentially corroded when the $\text{pH} < 4$ but the α phase dissolves first when the $\text{pH} > 4$. The results of Weill-Couly et al. [10] showed that the corrosion resistance of NAB in seawater was related to its microstructures. The phase transformation of a small amount of $\beta' \rightarrow \alpha + \kappa$ could effectively improve the corrosion resistance of the alloy in seawater. The excellent corrosion resistance of NAB is derived from a corrosion product film produced on the surface [4,11–14]. Schüssler et al. [4] proposed that the corrosion product film produced on the surface of NAB contained an inner layer of Al_2O_3 and an outer layer of Cu_2O ; furthermore, a thickness of 800–1000 nm could reduce the corrosion rate by 20–30 times. If time is sufficient, corrosion products such as $\text{Cu}_2(\text{OH})_3\text{Cl}$ will also form on the outer layer of the film [12,13].

The as-cast NAB pieces used for ship propellers are very large, weighing as much as 200 t. Therefore, cast defects are unavoidable. Large and concentrated defects can be repaired in various ways to reduce the adverse effects of defects. For example, Sabbaghzadeh et al. [15] repaired NAB by

fusion welding, and the galvanic corrosion current between the welded and the as-cast microstructures was only a few nA. Hanke et al. [16] applied a friction surface treatment for as-cast NAB, resulting in refinement and homogenization of the surface microstructure, which repaired cast defects. Ni et al. [17] used friction stir processing for as-cast Ni-Al bronze and compared the weight loss of the treated NAB and as-cast NAB in 3.5% NaCl solution. It was found that the weight loss of the treated NAB was significantly smaller than that of as-cast NAB, improving corrosion performance. That is, welding can improve the corrosion resistance of copper alloys with large cast defects in seawater.

However, for small and dispersed defects, they are not only unavoidable but also difficult to repair. Therefore, NAB propellers that are put into use generally have small cast defects, and their effect on the corrosion behavior of NAB in practical applications should be considered. Unfortunately, there is little literature available on this issue. Therefore, the effect of small cast defects on the corrosion behavior of the UNS C95810 alloy will be investigated in this paper by comparing the corrosion rate, morphology, product composition and electrochemical corrosion parameter of the specimen with and without defects.

2. Experiment

2.1. Materials and Corrosive Medium

The experimental material was UNS C95810 and its chemical composition is shown in Table 1.

Table 1. Composition of the UNS C95810.

Elements	Cu	Mn	Fe	Al	Ni	Zn, Sn, Pb, C, Si, P, Sb
UNS C95810 (wt.%)	79.9	1.39	4.8	9.24	4.43	Trace

The measured yield strength, tensile strength and elongation were 266 MPa, 679 MPa and 29.5%, respectively. Specimens with and without defects were taken from a UNS C95810 on a large as-cast sample, and they were cut out (of $10 \times 10 \times 10 \text{ mm}^3$) and observed under optical microscopy to determine whether there was a defect on the surface of each sample. For simplicity, the specimens with and without defects are represented by S-Defect and S-Cast, respectively. To effectively control the uncertainties of the test, artificial seawater was used as a corrosive medium, and its main chemical composition from ASTM D1141 was listed in Table 2.

Table 2. Chemical components of artificial seawater [18].

Components	NaCl	MgCl ₂	Na ₂ SO ₄	CaCl ₂	KCl	NaHCO ₃	KBr	H ₃ BO ₃	SrCl ₂	NaF
Mass Concentration (g/L)	24.53	5.2	4.09	1.16	0.695	0.201	0.101	0.027	0.025	0.003

2.2. Preparation of Test Specimens

2.2.1. Specimens for Electrochemical Tests

Each of the specimens was mounted in plastic tubes by a two-component epoxy resin (WSR618, Nantong Xingchen Synthetic Material Co., Ltd, Nantong, China) with a Cu wire welded on their back, leaving an area of 0.38 cm^2 to be in contact with the artificial seawater. The study surface of each specimen was ground to 1000 grit by silicon carbide abrasive paper and polished. Then, the sample was cleaned with absolute ethanol to remove organics, embedded polishing media, etc.

2.2.2. Specimens for the Corrosion Test and Microstructure Analysis

Each specimen used for the weight loss measurements, scanning electron microscopy (SEM, Supra-55-sapphire, Carl Zeiss AG, Jena, Germany), confocal laser scanning microscopy (CLSM, OLS4000, Olympus, Tokyo, Japan) and X-ray diffraction (XRD, D/MAX-Ultima+, Rigaku, Tokyo, Japan)

was mounted in plastic tubes by a two-component epoxy resin, leaving an area of 1 cm² to be in contact with the artificial seawater. The test surface of each specimen was ground to 1000 grit by silicon carbide abrasive paper and polished. Then, the sample was cleaned with absolute ethanol to remove organics, embedded polishing media, etc.

2.3. Measurement and Characterization

2.3.1. Weight Loss

The specimens prepared in 2.2.2 were ultrasonically cleaned in ethanol, dried with blowing air and weighed as m_1 . They were then immersed in artificial seawater. After immersion for 72 h, 168 h, 432 h, 720 h and 960 h, the specimens were removed, rinsed with deionized water, dried, and weighed as m_2 . Subsequently, they were immersed in HCl solution (containing 500 mL of commercially available 32% HCl and 500 mL of deionized water) for 2 min to remove the corrosion products and weighed as m_3 after ultrasonically cleaning and drying. The weight loss of a fresh sample after immersion in this solution for 2 min was less than 0.1 mg to ensure the base metal was not attacked vigorously by the acid. The weight loss of the specimen and the weight of the corrosion products were noted as $m_1 - m_3$ and $m_2 - m_3$, respectively. The weight loss rate = $\frac{m_1 - m_3}{S \cdot t}$, where S is the surface area of the sample in contact with artificial seawater and t is the immersion time.

2.3.2. Microstructure Analysis and Corrosion Morphology Observation

The surface morphology of the specimen prepared in as described in Section 2.2.2 was observed by SEM, and the defects and their surrounding as-cast microstructures were analyzed by an energy dispersive spectrometer (EDS, Ultim Extreme, OXFORD Instruments, Oxford, UK) before and after immersion in artificial seawater. After immersion for 72 h and 240 h, they were removed, rinsed with deionized water, dried, and observed by CLSM. After immersion in artificial seawater for 720 h, the washed and dried specimens were subjected to SEM observation and EDS analysis.

2.3.3. XRD

The specimens prepared in 2.2.2 were tested using an X-ray diffractometer (D/MAX-Ultima⁺, Rigaku, Tokyo, Japan) with Co K α radiation. The diffraction angle range was from 10° to 100°. The specimens that had been tested by XRD were immersed in artificial seawater. After immersion for 240 h and 720 h, they were removed, rinsed with deionized water, dried, and tested by XRD.

2.3.4. Electrochemical Test

Electrochemical measurements were conducted in a typical three-electrode system. The working electrode was the surface of the specimen with an area of 0.38 cm² prepared in 2.2.1. A platinum net and a saturated calomel electrode served as the counter and reference electrode, respectively. The test medium was 100 mL of artificial seawater. The polarization curves were recorded at a sweep rate of 1 mV/s from -500 mV to 500 mV vs. the open circuit potential using an IM6ex Electrochemical Workstation (IM6ex, ZAHNER, Kronach, Germany). The voltage perturbation was 10 mV. To avoid any inconsistency of the experiment, two or three repeated tests were carried out for each sample. The electrochemical corrosion parameters in this paper were then obtained by fitting a linear polarization region of approximately 10 mV around the resting potential [19].

3. Result

3.1. Weight Loss

The test results of S-Cast and S-Defect weight loss in artificial seawater are shown in Figures 1–3. The results show that the weight loss and film weight of S-Cast and S-Defect generally show a gradual increase trend with corrosion time but their weight loss rates gradually decrease with corrosion time.

Moreover, the weight loss, film weight and weight loss rate of S-Defect are larger than that of S-Cast. Therefore, the defects accelerate the corrosion of UNS C95810. Defects induce a discontinuous corrosion product film on NAB in seawater, which results in a decrease in the protective effect of the film on the substrate and an increase in the corrosion rate and the thickness of the film.

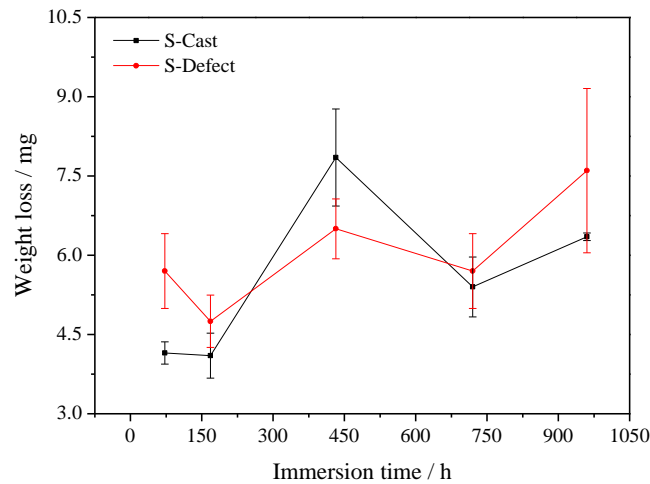


Figure 1. Weight loss of S-Cast and S-Defect immersed for different time periods in artificial seawater.

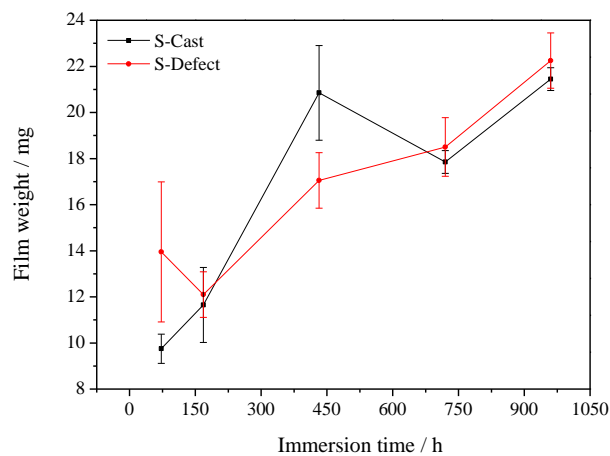


Figure 2. Film weight of S-Cast and S-Defect immersed for different time periods in artificial seawater.

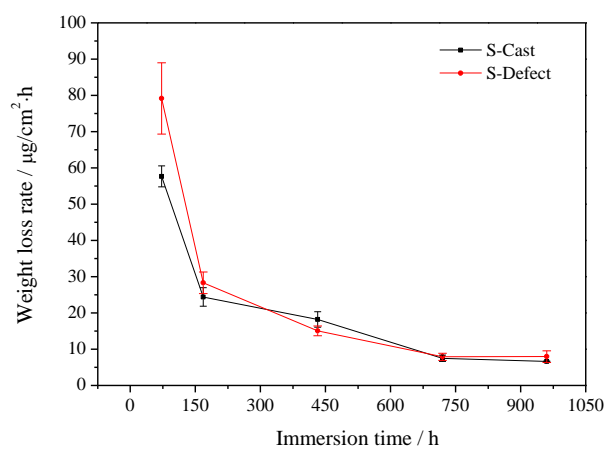


Figure 3. Weight loss rate of S-Cast and S-Defect immersed for different time periods in artificial seawater.

3.2. Microstructure and Corrosion Morphology

The normal microstructure of UNS C95810 is mainly composed of a α phase matrix and a dispersed κ phase (Figure 4).

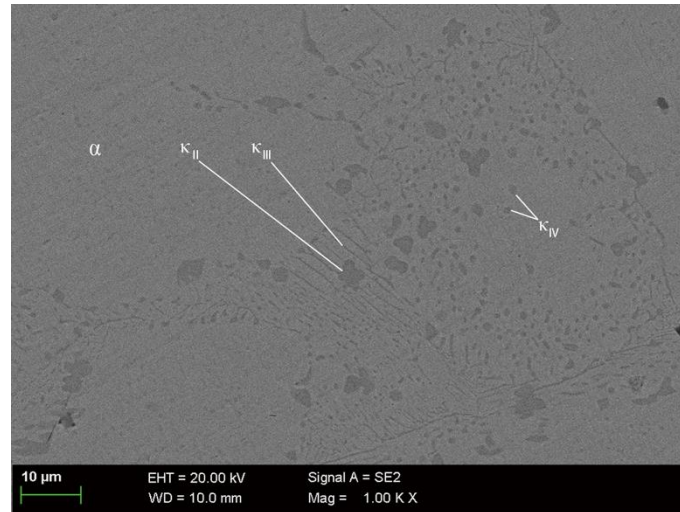


Figure 4. The microstructure of S-Cast before corrosion.

According to the composition and shape of the κ phase, it can be divided into κ_{II} , κ_{III} and κ_{IV} . The phase κ_{II} is an intermetallic compound based on Fe_3Al , which is flower-like or spherical with a size of 5 to 10 μm and distributed at the boundary of the α phase [9]. The κ_{III} phase is a lamellar intermetallic compound based on $NiAl$ [9]. The κ_{IV} phase is an intermetallic compound based on Fe_3Al and is distributed in the α phase with a size smaller than 2 μm [9]. The size of the α phase is generally more than 100 μm [20]. To determine the chemical composition of the defects, EDS tests of selected area and selected points (Figure 5) are carried out. The results show that there is only copper in selected point while there are many oxygen and few chlorine elements in alloys in selected areas, as shown in Table 3.

Table 3. The composition of the studied specimens by SEM with EDS.

Specimen	Content of Element (atom.%)						
	O	Al	Si	S	Cl	Fe	Cu
Selected point in Figure 5							100
Selected area in Figure 5	59.29	13.39	4.09	1.68	1.59	1.64	18.32

It can be inferred that the microstructures in defects mainly include pure copper, an oxide of copper and aluminum and the κ phase.

S-Cast and S-Defect differ in their corrosion processes. S-Cast is preferentially corroded at the boundary of the α phase and some locations within the α phase, and the corrosion near the boundary of the α phase is more serious (Figure 6a,b).

As the corrosion progresses, the α phase also begins to undergo significant corrosion (Figure 6c,d). When the corrosion reaches 30 days, obvious corrosion products have formed on the surface of the alloy (Figure 6e). S-Defect is preferentially corroded at the defects, and the corrosion near the defects is more serious (Figure 7a,b).

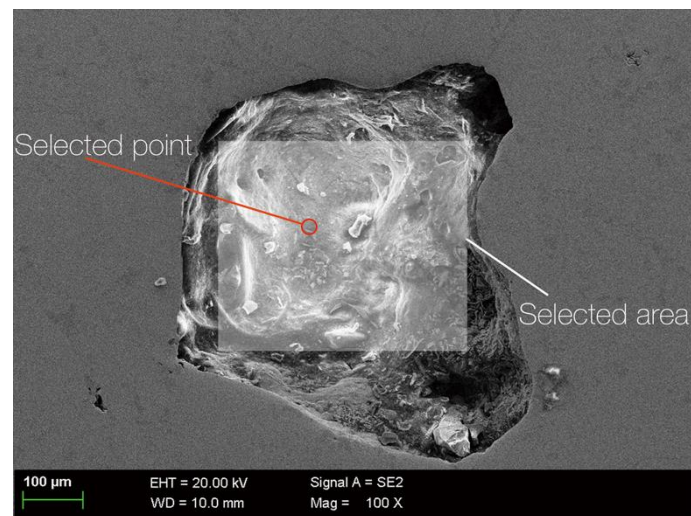


Figure 5. Surface and point scan of S-Defect before corrosion.

After the corrosion occurs at the defects and their vicinity, the corrosion at the α phase boundary and some locations within the α phase gradually becomes apparent (Figure 7a–d). When the corrosion reaches 30 days, a large area of severe corrosion is occurred at the defects compared to other locations (Figure 7e). In addition to affecting the location of preferential corrosion, defects increase the complexity of UNS C95810 microstructures, leading to an increase in tendency toward galvanic corrosion, thus accelerating the corrosion of UNS C95810 (Figure 6 vs. Figure 7). To determine whether there is a difference between the corrosion product composition of the defects and that of the surrounding as-cast microstructures, EDS analysis is performed on the position shown in Figure 7e. The results (Table 4) show that there is almost no composition difference between the corrosion product of the defects and that of the surrounding as-cast microstructures.

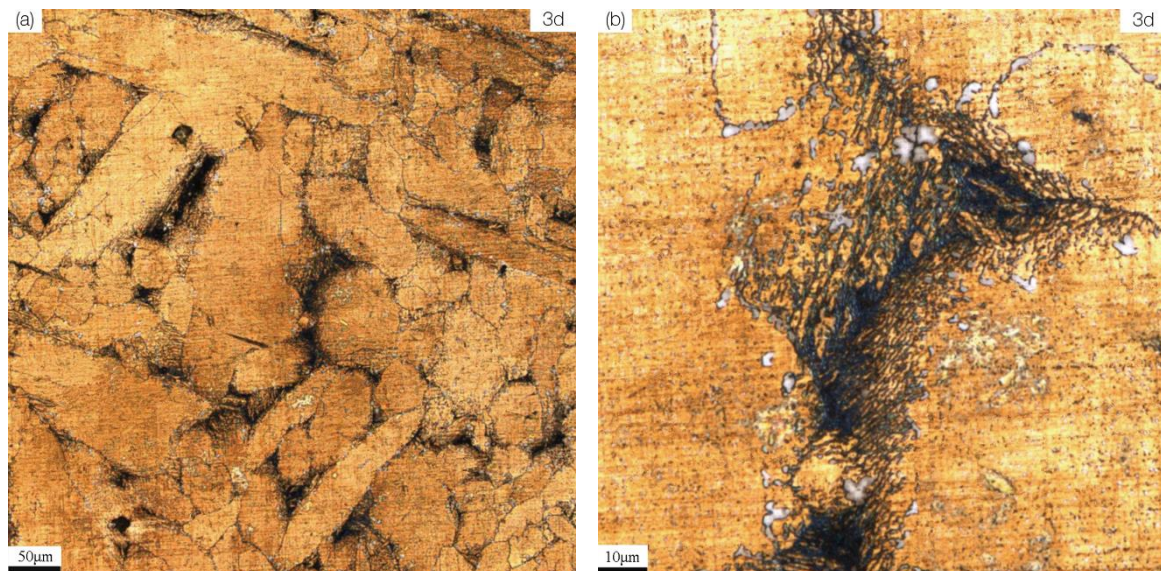


Figure 6. Cont.

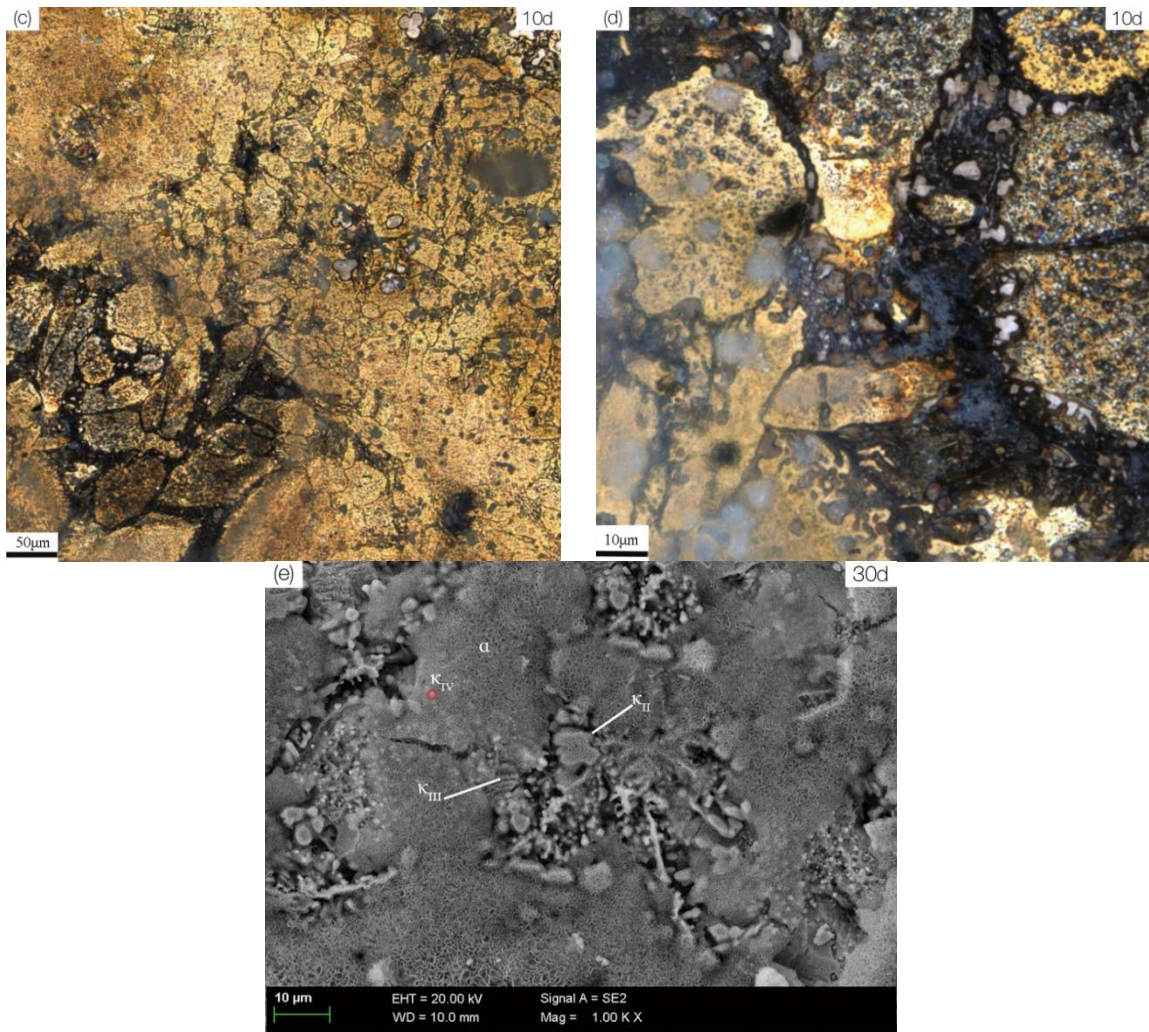


Figure 6. The corrosion morphology of for S-Cast immersed in artificial seawater at different times: (a) 3 d; (b) local magnification at 3 d; (c) 10 d; (d) local magnification at 10 d; (e) 30 d.

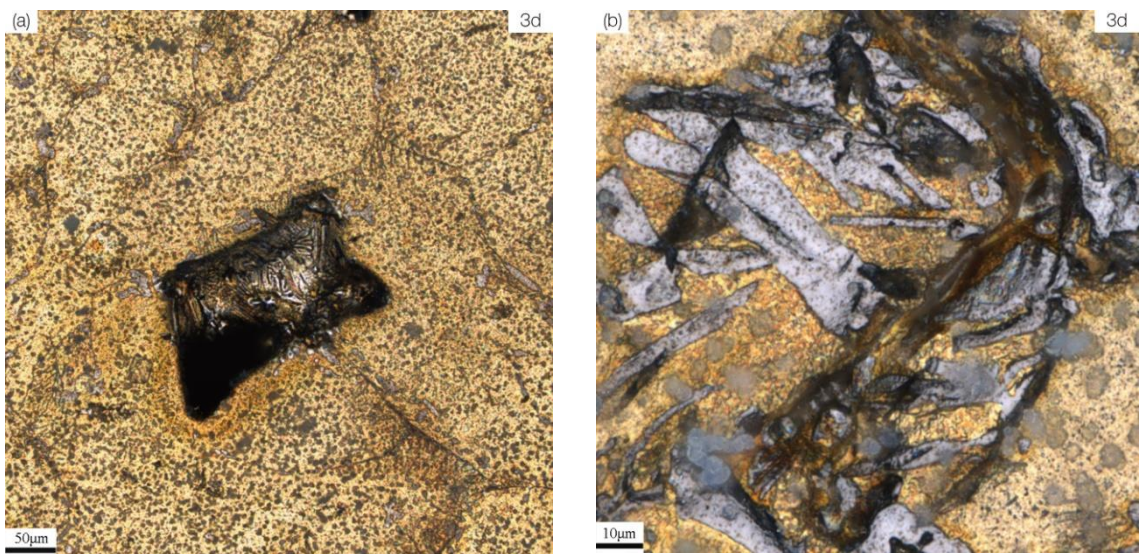


Figure 7. Cont.

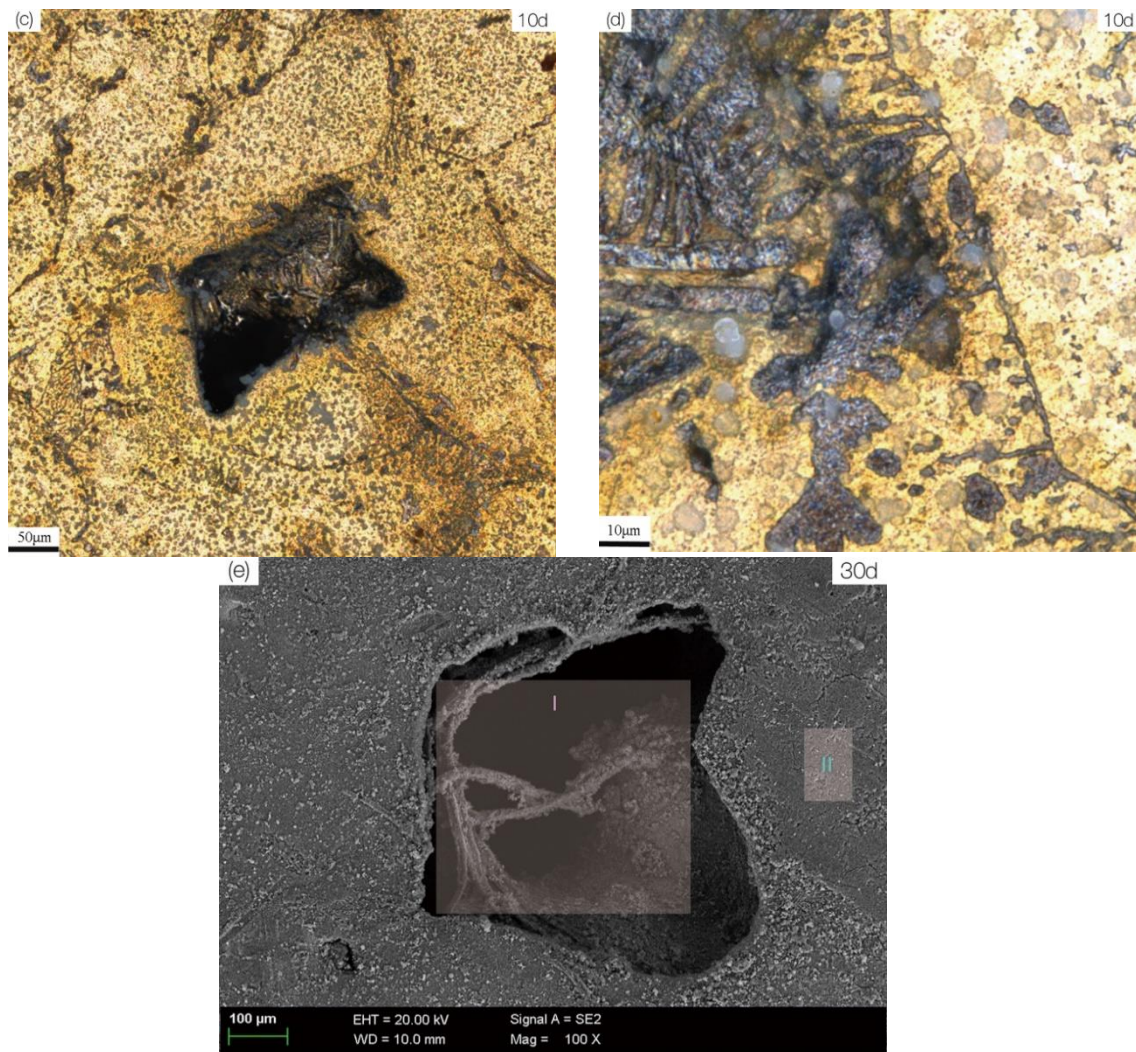


Figure 7. The corrosion morphology of for S-Defect immersed in artificial seawater at different times: (a) 3 d; (b) local magnification at 3 d; (c) 10 d; (d) local magnification at 10d; (e) 30 d.

Table 4. The composition of the studied position by SEM with EDS.

Position	Content of Element (atom.%)								
	O	Mg	Al	S	Cl	Ca	Fe	Ni	Cu
Zone I in Figure 7e	78.79		2.99	1.30	3.43	0.85	0.85		11.79
Zone II in Figure 7e	72.01	2.31	6.62	1.38	3.67	0.29	0.47	1.13	12.12

3.3. Corrosion Product Film

The XRD results of S-Defect and S-Cast for different immersion periods are shown in Figures 8 and 9. Cu_2O , $\text{Cu}(\text{OH},\text{Cl})_2$ and $\text{Cu}_2(\text{OH})_3\text{Cl}$ are detected in the XRD results of S-Defect and S-Cast. Cu_2O changes little with corrosion while $\text{Cu}(\text{OH},\text{Cl})_2$ and $\text{Cu}_2(\text{OH})_3\text{Cl}$ vary greatly with corrosion (Figure 8). $\text{Cu}(\text{OH},\text{Cl})_2$ is more abundant in the corrosion products after 10 days than that of $\text{Cu}_2(\text{OH})_3\text{Cl}$ (Figure 8). Therefore, it is considered that during the corrosion process, Cu dissolves to Cu^+ , and then it reacts with Cl^- to form CuCl_2^- [13,20].

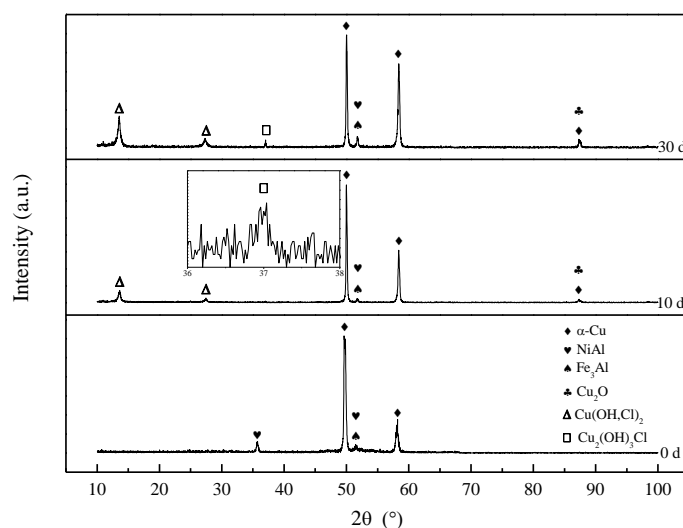


Figure 8. The XRD patterns of S-Defect immersed for different time periods in artificial seawater.

Over time, it converts to Cu_2O [20,21]. As the amount of Cu_2O increases, it will react with Cl^- to form more stable phases, such as $\text{Cu}_2(\text{OH})_3\text{Cl}$ [20–22]. This is similar to the experimental results of Song [21] and Du [22]. Song [21] proposed that $\text{Cu}_2(\text{OH})_3\text{Cl}$ was located on the outermost layer of a NAB corrosion product film. Du [22] proposed that $\text{Cu}(\text{OH})_2$ and CuCl_2 were located between Cu_2O and $\text{Cu}_2(\text{OH})_3\text{Cl}$. It is believed that since Al is more active than Cu, it first dissolves to form Al_2O_3 , and then Cu dissolves to form CuO and Cu_2O . $\text{Cu}(\text{OH})_2$, CuCl_2 and $\text{Cu}_2(\text{OH})_3\text{Cl}$ are formed on the basis of products formed by the dissolution of Cu. Therefore, they should be located on the outer layers of the Al_2O_3 , CuO and Cu_2O . The XRD results in this study indicate that the Al_2O_3 , Cu_2O , CuO , $\text{Cu}(\text{OH})_2$, CuCl_2 and $\text{Cu}_2(\text{OH})_3\text{Cl}$ phases were detected on the corrosion product film with increasing corrosive time. In summary, the corrosion product film of UNS C95810 has a three-layer structure.

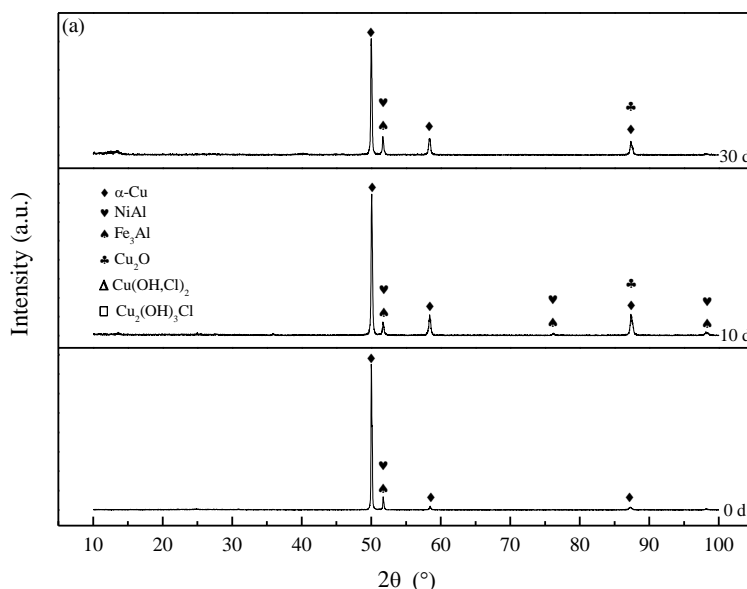


Figure 9. Cont.

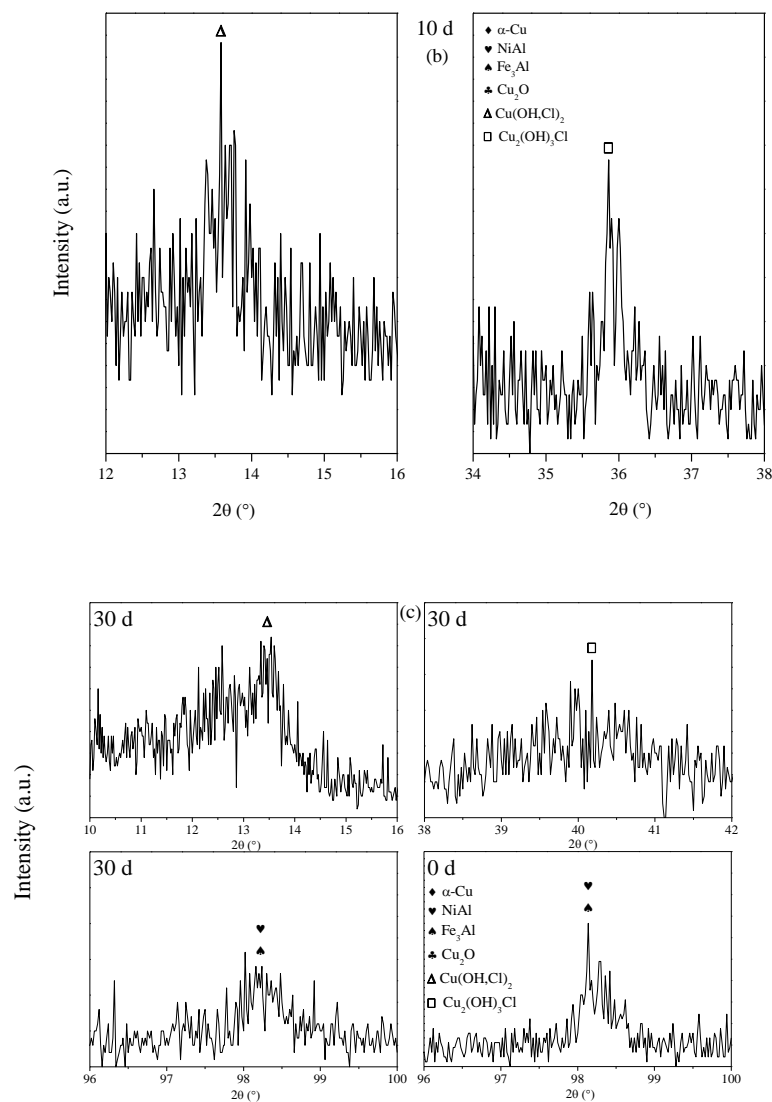


Figure 9. The XRD patterns of (a) S-Cast immersed for different time periods in artificial seawater and (b,c) S-Cast partial magnification.

3.4. Electrochemistry

The polarization curves of S-Cast and S-Defect in artificial seawater are shown in Figure 10.

The electrochemical corrosion parameters obtained by fitting a linear polarization region of approximately 10 mV around the resting potential are shown in Table 5.

The corrosion potential and corrosion current density of S-Defect are -86.31 mV and $0.23 \mu\text{A}\cdot\text{cm}^{-2}$, respectively, while those of S-Cast are -3.83 mV and $0.228 \mu\text{A}\cdot\text{cm}^{-2}$, respectively. Generally, defects decrease the corrosion potential and increase the corrosion current density. Defects increase the tendency toward galvanic corrosion of UNS C95810, which leads to the promotion of the corrosion driving force, thus accelerating corrosion. Therefore, S-Defect has a lower corrosion potential and a larger corrosion current density than those of S-Cast.

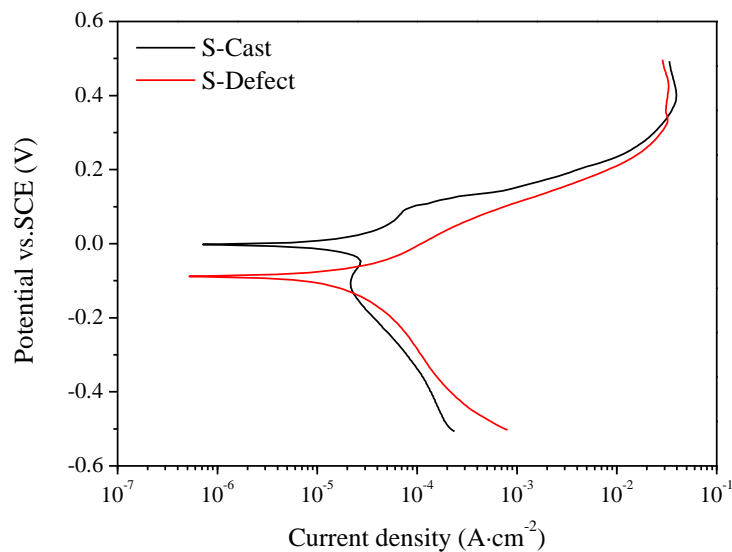


Figure 10. The polarization curve of S-Cast and S-Defect.

Table 5. Corrosion parameters of S-Cast and S-Defect.

Sample	Mean (Standard Deviation)		
	Potential vs. SCE (mV)	Current Density ($\mu\text{A}\cdot\text{cm}^{-2}$)	R_p ($\text{k}\Omega\cdot\text{cm}^2$)
S-Cast	-3.83 (1.93)	0.228 (0.12)	18.9 (2.12)
S-Defect	-86.31 (3.62)	0.23 (0.22)	14.9 (2.89)

4. Discussion

4.1. Corrosion Rate of UNS C95810

Defects can affect the diffusion of Cl^- and the corrosion driving force, thus accelerating the corrosion of NAB. The presence of defects causes the passivation film formed on NAB to become uneven. Generally, the electric field strength in the passivation film (ϵ) obeys the following formula: $\epsilon = \frac{V}{l}$, where V is the potential difference between the two sides of the passivation film and l is the thickness of the passivation film [19]. Because the passivation film at the defects is thinner than that at other locations [19], the field strength at the defects is higher than that at other locations. This causes Cl^- to diffuse more easily to the defects and to enrich there (Figure 11 and Table 6), resulting in faster destruction of the passivation film.

Table 6. The composition of S-Defect immersed in artificial seawater for 3 h.

Specimen	Content of Element (atom.%)						
	O	Al	Mn	Cl	Fe	Ni	Cu
Position I	73.30	3.33	-	2.13	2.90	1.44	16.90
Position II	-	15.07	1.41	-	2.65	2.33	78.54
Position III	-	29.27	2.6	-	46.35	12.96	8.82

Once the passivation film is broken, the substrate is directly in contact with the corrosive medium, which accelerates the corrosion rate. Therefore, the presence of defects affects the diffusion of Cl^- and the corrosion process.

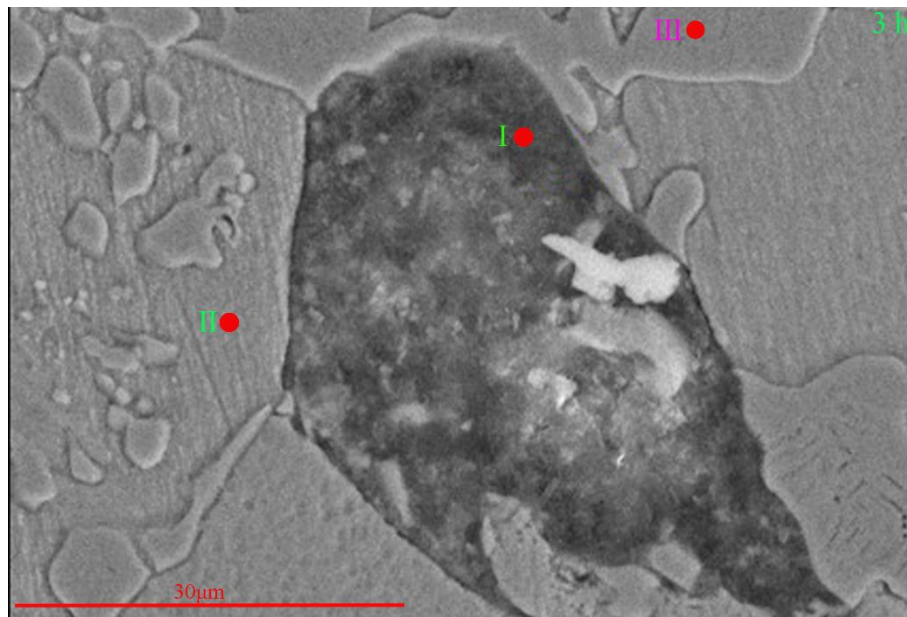
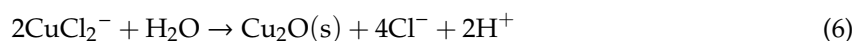
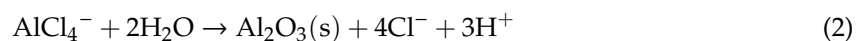


Figure 11. SEM image of S-Defect immersed in artificial seawater for 3 h.

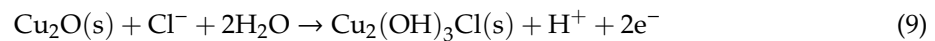
4.2. Corrosion Product Film Structure of S-Defect

The results of the XRD test show that the X-ray diffraction pattern of both the S-Cast and S-Defect samples are basically the same, as shown in Figures 8 and 9, but the intensity of some phases in the corrosion products is different. Therefore, they have similar corrosion product film structures but different corrosion product film thicknesses (Figures 2, 8 and 9). It had been reported that a corrosion product film with Cu_2O in the outer layer and Al_2O_3 in the inner layer was formed on a NAB [4] and a ternary Cu-Al-Ni alloy [23,24]. Cu_2O and Al_2O_3 were formed by the following reactions [12,13,22,24,25]:



Cu_2O is a p-type semiconductor with cation vacancies. It can accept foreign ions, such as Ni and Fe ions, to incorporate into inner cation vacancies, further improving the protection from the film [14,26,27]. Based on previous research [4,14,21,23,24,26,27], Cu_2O should be the main corrosion product in the inner layer of the film for both S-Cast and S-Defect. Fe and Ni is enriched in the inner layer by incorporating into the lattice of Cu_2O . The microstructures of the S-Cast and S-Defect are complex, resulting in different Cu dissolution rates in different phases. Because Al_2O_3 cannot form simultaneously on different phases, the discontinuous Al_2O_3 layer on the surface is not impermeable to the passage of cuprous cations [20]. As a result, the inner layer of the corrosion product film consists of Al_2O_3 and Cu_2O with the incorporation of Fe and Ni [20]. In the XRD tests, $\text{Cu}(\text{OH},\text{Cl})_2$ and $\text{Cu}_2(\text{OH})_3\text{Cl}$ are detected in the corrosion products of S-Cast and S-Defect. They could form by the following reactions [13,25,26,28]:





According to Song's research [21] on a NAB corrosion product film, $\text{Cu}_2\text{(OH)}_3\text{Cl}$ was located in the outer layer of the NAB corrosion product film. In the structure of the NAB corrosion product film proposed by Du [22], Cu(OH)_2 or CuO was located between Cu_2O and $\text{Cu}_2\text{(OH)}_3\text{Cl}$. Therefore, combined with the above analysis and the results of the XRD test, it can be concluded that the structure of the S-Defect corrosion product film is as follows (Figure 12): the inner layer is Al_2O_3 and Cu_2O with the incorporation of Fe and Ni, the middle layer is Cu(OH,Cl)_2 or CuO , and the outer layer is $\text{Cu}_2\text{(OH)}_3\text{Cl}$.

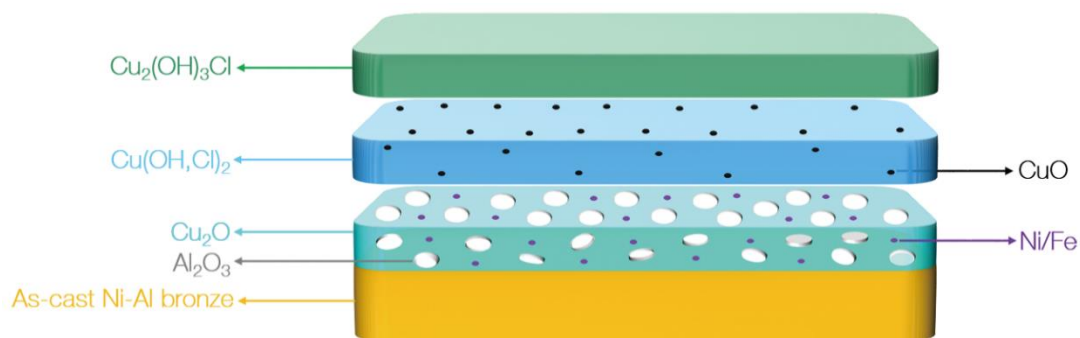


Figure 12. The corrosion product film structure of S-Defect immersed in artificial seawater for a long time.

4.3. Microstructure and Corrosion Behavior of UNS C95810

The stability of the phase and its corrosion products can affect the corrosion behavior, and the stability of the phase can be expressed with a work function. There is a corresponding relationship between work function and Volta potential: $V_{CPD} = (\Phi_{tip} - \Phi_{sample})/e$, where V_{CPD} is the Volta potential, Φ_{tip} and Φ_{sample} are the work functions of the tip and the sample, respectively, and e is the value of the electronic charge [29]. The value of Φ_{tip} is constant. Thus, higher V_{CPD} results in lower Φ_{sample} . The work function is defined as the minimum energy required for an electron to escape from the surface of a solid. A lower work function of a material represents more likely occurrences of corrosion [30]. Therefore, a substance with a higher Volta potential is more susceptible to corrosion. From the measurements of the Volta potential of an as-cast NAB by Song, it can be seen that the Volta potential of the κ_{IV} phase was higher than that of the α phase but lower than that of the κ_{II} phase [21]. Hence, the stability of the phases from low to high should be κ_{II} , κ_{IV} and α . However, in near-neutral artificial seawater, Al_2O_3 is formed on the surface of the Al-rich κ phase and its stability is much higher than that of Cu_2O , so the κ phase as the cathode phase will not continue to corrode but accelerates the corrosion rate of the surrounding microstructures [31]. Since the κ_{IV} phase and κ_{II} phase are located in the α phase and the boundary of the α phase, corrosion preferentially occurs in the α phase boundary and some locations in the α phase. The Volta potential between the κ_{II} phase and α phase is 60–80 mV, while that between the κ_{IV} phase and α phase is 20–40 mV [21]. The areas with a higher Volta potential have a stronger driving force for corrosion. Therefore, the corrosion in the α phase boundary is more prone to occur than that in the α phase.

The existence of defects accelerates the corrosion process to a certain extent, mainly due to the following reasons. First, the defect microstructures mainly include oxides of copper and aluminum, along with pure copper. This is a more complex phase composition than the as-cast microstructures. Such a phase composition makes it easier for the inside of defects and between the defects and the surrounding microstructures to form a galvanic corrosion, thereby accelerating the corrosion of the defects and the microstructures near the defects. Second, defects not only make the microstructures

of as-cast NAB more complex but also cause the inhomogeneity of the corrosion product film, resulting in greater stress in the growth process of the film [21]. The increase in growth stress can cause the film to become loose or even crack, thereby causing the corrosive medium to more easily enter the film and corrode the substrate. Finally, the corrosion potential of UNS C95810 decreases due to defects. The lower corrosion potential provides a more powerful driving force for corrosion, thereby accelerating the corrosion of UNS C95810.

4.4. Corrosion Mechanism of UNS C95810

According to the experimental results obtained in this paper and related literature [21], the stability of the phases in NAB from low to high is κ_{II} , κ_{IV} , κ_{III} and. Since the κ phase is an Al-rich phase and Al is a more active metal than Cu, the κ phase will preferentially corrode and form Al_2O_3 on the surface when NAB is in contact with seawater. Al_2O_3 is a more stable oxide than that of Cu_2O and CuO , so the κ phase covered by Al_2O_3 will no longer corrode as an anode phase but will act as a cathode phase in galvanic corrosion to accelerate the corrosion of the surrounding microstructures. The above results in the formation of Cu_2O , $Cu(OH,Cl)_2$ and $Cu_2(OH)_3Cl$ on the surface of the surrounding microstructures. The Volta potential between the κ_{II} , κ_{III} , κ_{IV} phases and the α phase is 60–80 mV, 10–30 mV and 20–40 mV, respectively [21]. Therefore, the corrosion near the κ_{II} phase is the fastest and the most serious, followed by that near the κ_{IV} phase, and finally that near the κ_{III} phase. In summary, the specific corrosion behavior of S-Cast can be summarized as Figure 13.

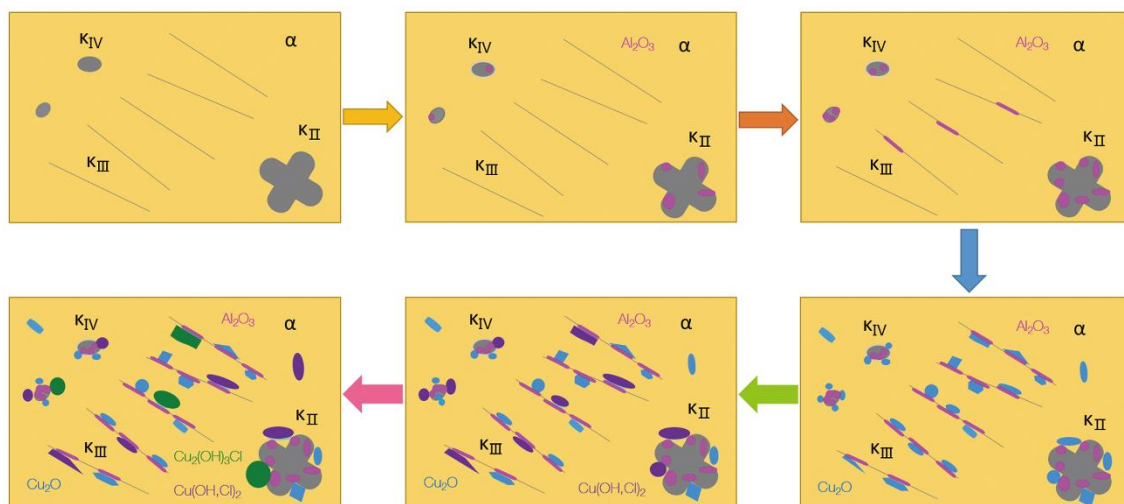


Figure 13. Process mechanism of corrosion behavior of S-Cast immersed in artificial seawater.

For S-Defect, in addition to the corrosion characteristics of S-Cast, it has some additional characteristics due to the presence of defects. The presence of defects not only promotes the formation of galvanic corrosion between the internal microstructures of the defects but also promotes that between the defects and the surrounding microstructures, thereby greatly increasing the tendency toward galvanic corrosion. Therefore, the corrosion behavior of S-Defect can be obtained by combining the corrosion process of S-Cast with an additional galvanic corrosion process introduced due to the existence of defects. Its corrosion mechanism can be summarized as shown in Figure 14.

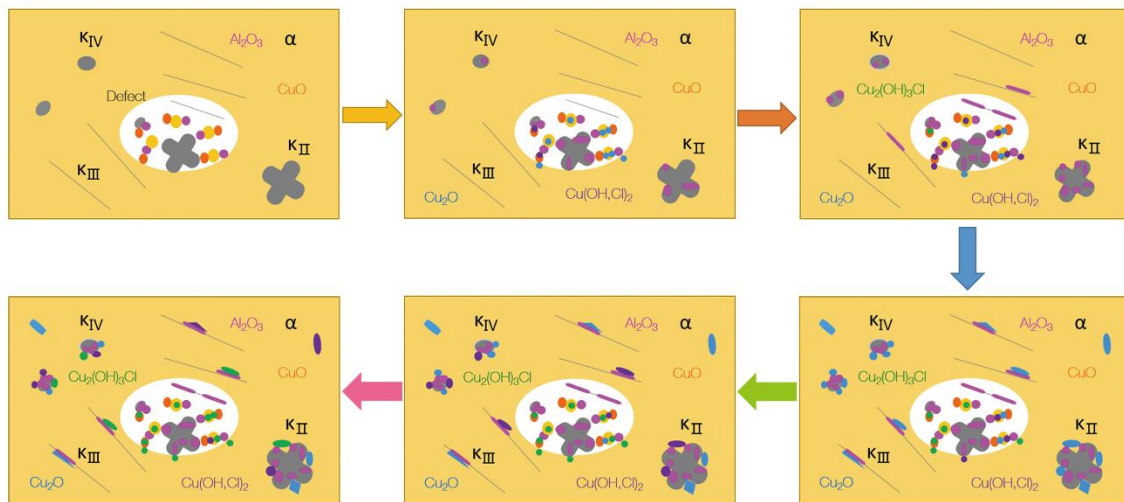


Figure 14. Process mechanism of corrosion behavior of S-Defect immersed in artificial seawater.

5. Conclusions

In this paper, the effects of cast defects on the corrosion behavior and mechanism of the UNS C95810 in artificial seawater were studied. The conclusions are as follows:

- 1) The microstructure of the UNS C95810 alloy consists of an α phase and a κ phase. Except for these cast phases, there are oxides of copper and aluminum, along with pure copper in defects.
- 2) Compared to those of S-Cast, S-Defect has a thicker corrosion product film, more negative corrosion potential and greater corrosion current density.
- 3) The corrosion product film of both S-Defect and S-cast consists of three layers. The inner layer is Al_2O_3 and Cu_2O with the incorporation of Fe and Ni, the middle layer is $\text{Cu}(\text{OH},\text{Cl})_2$ or CuO , and the outer layer is $\text{Cu}_2(\text{OH})_3\text{Cl}$. The defects do not affect the phase composition of the corrosion products, but they have an effect on the amount of the specific phase in the corrosion products.

Author Contributions: Conceptualization, X.Z., Y.Q. and Z.Z.; methodology, X.Z., Y.Q. and Z.Z.; software, X.Z.; validation, J.W.; formal analysis, X.Z. and Z.Z.; investigation, X.Z. and Z.Z.; resources, J.Z., L.Q., D.H., Y.Q. and Z.Z.; data curation, X.Z.; writing—original draft preparation, X.Z.; writing—review and editing, X.Z., Z.Z. and Y.Q.; visualization, X.Z. and J.W.; supervision, Z.Z. and Y.Q.; project administration, Z.Z. and Y.Q.; funding acquisition, Z.Z. and Y.Q. All authors have read and agreed to the published version of the manuscript.

Funding: This research was funded by Project of Equipment Pre-research Field Fund, grant number 61409220304 and Equipment Pre-research Sharing Technology Project, grant number 41404010306,41423060314.

Acknowledgments: Thanks to Zeng Kai for his help in the experimental part of this article.

Conflicts of Interest: The authors declare no conflict of interest.

References

1. Culpan, E.A.; Rose, G. Corrosion Behaviour of Cast Nickel Aluminium Bronze in Sea Water. *Br. Corros. J.* **2014**, *14*, 160–166. [[CrossRef](#)]
2. Al-Hashem, A.; Caceres, P.G.; Shalaby, H.M.; Riad, W.T. Cavitation Corrosion Behavior of Cast Nickel-Aluminum Bronze in Seawater. *Corrosion* **1995**, *51*, 331–342. [[CrossRef](#)]
3. Wharton, J.A.; Barik, R.C.; Kear, G.; Wood, R.J.K.; Stokes, K.R.; Walsh, F.C. The corrosion of nickel-aluminium bronze in seawater. *Corros. Sci.* **2005**, *47*, 3336–3367. [[CrossRef](#)]
4. Schüssler, A.; Exner, H.E. The corrosion of nickel-aluminium bronzes in seawater—I. Protective layer formation and the passivation mechanism. *Corros. Sci.* **1993**, *34*, 1793–1802. [[CrossRef](#)]
5. Schüssler, A.; Exner, H.E. The corrosion of nickel-aluminium bronzes in seawater—II. The corrosion mechanism in the presence of sulphide pollution. *Corros. Sci.* **1993**, *34*, 1803–1811. [[CrossRef](#)]

6. Ferrara, R.J.; Caton, T.E. Review of dealloying of cast aluminum bronze and nickel-aluminum bronze alloys in sea water service. *Mater. Perform.* **1982**, *21*, 30–34.
7. Neodo, S.; Carugo, D.; Wharton, J.A.; Stokes, K.R. Electrochemical behaviour of nickel–aluminium bronze in chloride media: Influence of pH and benzotriazole. *J. Electroanal. Chem.* **2013**, *695*, 38–46. [[CrossRef](#)]
8. Lorimer, G.W.; Hasan, F.; Iqbal, J.; Ridley, N. Observation of microstructure and corrosion behaviour of some aluminium bronzes. *Br. Corros. J.* **2013**, *21*, 244–248. [[CrossRef](#)]
9. Hasan, F.; Jahanafrooz, A.; Lorimer, G.W.; Ridley, N. The morphology, crystallography, and chemistry of phases in as-cast nickel-aluminum bronze. *Metall. Trans. A* **1982**, *13*, 1337–1345. [[CrossRef](#)]
10. Weill-Couly, P.; Arnaud, D. Effect of the Composition and Structure of Aluminum Bronzes on their Behavior in Service. *Fonderie* **1973**, 123–135.
11. Tuthill, A.H. Guidelines for the use of copper alloys in seawater. *Mater. Perform.* **1987**, *26*, 12–22.
12. Ateya, B.G.; Ashour, E.A.; Sayed, S.M. Corrosion of $\hat{1}\pm\text{Al}$ bronze in saline water. *J. Electrochem. Soc.* **1994**, *141*, 71–77. [[CrossRef](#)]
13. Kato, C.; Castle, J.E.; Ateya, B.G.; Pickering, H.W. On the mechanism of corrosion of Cu-9.4Ni-1.7Fe alloy in air saturated aqueous NaCl solution 2. Composition of the protective surface layer. *J. Electrochem. Soc.* **1980**, *127*, 1897–1903. [[CrossRef](#)]
14. North, R.F.; Pryor, M.J. The influence of corrosion product structure on the corrosion rate of Cu-Ni alloys. *Corros. Sci.* **1970**, *10*, 297–311. [[CrossRef](#)]
15. Sabbaghzadeh, B.; Parvizi, R.; Davoodi, A.; Moayed, M.H. Corrosion evaluation of multi-pass welded nickel–aluminum bronze alloy in 3.5% sodium chloride solution: A restorative application of gas tungsten arc welding process. *Mater. Des.* **2014**, *58*, 346–356. [[CrossRef](#)]
16. Hanke, S.; Fischer, A.; Beyer, M.; Santos, J.D. Cavitation erosion of NiAl-bronze layers generated by friction surfacing. *Wear* **2011**, *273*, 32–37. [[CrossRef](#)]
17. Ni, D.R.; Xiao, B.L.; Ma, Z.Y.; Qiao, Y.X.; Zheng, Y.G. Corrosion properties of friction–stir processed cast NiAl bronze. *Corros. Sci.* **2010**, *52*, 1610–1617. [[CrossRef](#)]
18. Wang, J.; Yan, F.; Xue, Q. Tribological behaviors of some polymeric materials in sea water. *Sci. Bull.* **2009**, *54*, 4541–4548. [[CrossRef](#)]
19. Cao, C.N. *Principles of Electrochemistry of Corrosion*, 3rd ed.; Chemical Industry Press: Beijing, China, 2008.
20. Song, Q.N.; Zheng, Y.G.; Ni, D.R.; Ma, Z.Y. Characterization of the Corrosion Product Films Formed on the As-Cast and Friction-Stir Processed Ni-Al Bronze in a 3.5 wt% NaCl Solution. *Corrosion* **2015**, *71*, 606–614. [[CrossRef](#)]
21. Song, Q.N. Effect of Friction Stir Processing on the Cavitation Erosion and Corrosion Behaviors of As-Cast Ni-Al Bronze. Ph.D. Thesis, University of Chinese Academy of Sciences, Beijing, China, 2015.
22. Du, C.Y. Research on Corrosion Resistance of the Nickel-Aluminum Bronze and the Surface Treatment on It. Master’s Thesis, Jiangsu University of Science and Technology, Zhenjiang, China, 2014.
23. Badawy, W.A.; Al-Kharafi, F.M.; El-Azab, A.S. Electrochemical behaviour and corrosion inhibition of Al, Al-6061 and Al-Cu in neutral aqueous solutions. *Corros. Sci.* **1999**, *41*, 709–727. [[CrossRef](#)]
24. Nady, H.; Helal, N.H.; El-Rabee, M.M.; Badawy, W.A. The role of Ni content on the stability of Cu–Al–Ni ternary alloy in neutral chloride solutions. *Mater. Chem. Phys.* **2012**, *134*, 945–950. [[CrossRef](#)]
25. Mansfeld, F.; Liu, G.; Xiao, H.; Tsai, C.H.; Little, B.J. The corrosion behavior of copper alloys, stainless steels and titanium in seawater. *Corros. Sci.* **1994**, *36*, 2063–2095. [[CrossRef](#)]
26. Popplewell, J.M.; Hart, R.J.; Ford, J.A. The effect of iron on the corrosion characteristics of 90-10 cupro nickel in quiescent 3.4%NaCl solution. *Corros. Sci.* **1973**, *13*, 295–309. [[CrossRef](#)]
27. Milošev, I.; Metikoš-Huković, M. The behaviour of Cu-xNi (x = 10 to 40 wt%) alloys in alkaline solutions containing chloride ions. *Electrochim. Acta* **1997**, *42*, 1537–1548. [[CrossRef](#)]
28. Lenglet, M.; Lopitiaux, J.; Leygraf, C.; Odnevall, I.; Carballeira, M.; Noualhaguet, J.C.; Guinement, J.; Gautier, J.; Boissel, J. Analysis of corrosion products formed on copper in Cl₂/H₂S/NO₂ exposure. *J. Electrochem. Soc.* **1995**, *142*, 3690–3696. [[CrossRef](#)]
29. Li, M.; Guo, L.Q.; Qiao, L.J.; Bai, Y. The mechanism of hydrogen-induced pitting corrosion in duplex stainless steel studied by SKPFM. *Corros. Sci.* **2012**, *60*, 76–81. [[CrossRef](#)]

30. Li, W.; Li, D.Y. Variations of work function and corrosion behaviors of deformed copper surfaces. *Appl. Surf. Sci.* **2005**, *240*, 388–395. [[CrossRef](#)]
31. Wharton, J.A.; Stokes, K.R. The influence of nickel–aluminium bronze microstructure and crevice solution on the initiation of crevice corrosion. *Electrochim. Acta* **2008**, *53*, 2463–2473. [[CrossRef](#)]



© 2020 by the authors. Licensee MDPI, Basel, Switzerland. This article is an open access article distributed under the terms and conditions of the Creative Commons Attribution (CC BY) license (<http://creativecommons.org/licenses/by/4.0/>).